Supplementary Materials

Advancing Cellular Transfer Printing: Achieving Bioadhesion-Free Deposition via Vibration Microstreaming

Ziyu Huang[a], Yinning Zhou*[a]✉, Yu Liu[a], Yue Quan[a], Qiu Yin[b,c], Yucheng Luo[b], Yimeng Su[b], Bingpu Zhou[a], Wenming Zhang[c], Benpeng Zhu[d], Zhichao Ma*[b]✉

[a]Joint Key Laboratory of the Ministry of Education, Institute of Applied Physics and Materials Engineering, University of Macau, Avenida da Universidade, Taipa, Macau 999078, China

[b]Institute of Medical Robotics, School of Biomedical Engineering, Shanghai Jiao Tong University, No.800 Dongchuan Road, Shanghai 200240, China

[c]State Key Laboratory of Mechanical System and Vibration, Shanghai Jiao Tong University, Shanghai 200240, China

[d]School of Integrated Circuit, Wuhan National Laboratory for Optoelectronics, Huazhong University of Science and Technology, Wuhan 430074, China

*** Corresponding author**

E-mail addresses: ynzhou@um.edu.mo (Y. Zhou); zhichaoma@sjtu.edu.cn (Z. Ma)

1. Acoustic Streaming simulation Mechanism and Methods

The simulation was executed employing a numerical methodology, the credibility of which was established and authenticated in the study conducted by Muller et al. [1].

With the bulk acoustic actuation, liquid perturbations can be described by the following variables: temperature T, pressure p and velocity $\boldsymbol{v}$. Taking first and second order (subscript 1 and 2, respectively) into account, the above variables can be expressed as [1, 2]:

$$T = T_0 + T_1 + T_2$$

$$p = p_0 + p_1 + p_2$$

$$\boldsymbol{v} = \boldsymbol{v_1} + \boldsymbol{v_2}$$

where, T_0 and p_0 are the constant temperature and pressure before the presence of acoustic wavs. Meanwhile, $T = T_0$ and $\boldsymbol{v} = 0$, on all walls.

The temperature of each boundary condition is out of consideration. The acoustic source is modeled as the boundary condition using the first-order velocity $\boldsymbol{v_1}$ [1, 2]:

$$n \cdot \boldsymbol{v_1} = v_a e^{-iwt}$$

where n is the normal vector, v_a is the velocity magnitude at the actuated boundary and w is the angular frequency characterizing the harmonic time dependence.

As the first step, utilization of the thermos-viscous acoustic module within the frequency domain allows for the extraction of the primary acoustic field. Consequently, the first-order equation can be articulated as follows [1]:

$$i\omega T + \gamma D \nabla^2 T = \frac{\gamma - 1}{\alpha} \nabla \cdot \boldsymbol{v_1}$$

$$i\omega \rho_f \boldsymbol{v_1} + \mu \nabla^2 \boldsymbol{v_1} + \mu \left[\beta + i \frac{1}{\gamma k \mu \omega}\right] \nabla(\nabla \cdot \boldsymbol{v_1}) = \frac{\alpha}{\gamma k} \nabla T$$

where γ is the specific heat capacity ratio, D is the thermal diffusivity, ρ_f is the fluid density, μ

is the fluid dynamic viscosity, k is the fluid compressibility and β is the viscosity ratio.

The second-order acoustic can be obtained by employing the laminar flow module based on the calculate $\boldsymbol{v_1}$ and ρ_1 in the first order acoustic fields:

$$\rho_f \nabla \cdot \langle \boldsymbol{v_2} \rangle = -\nabla \cdot \langle \rho_1 \boldsymbol{v_1} \rangle$$

$$\mu \nabla^2 \langle \boldsymbol{v_2} \rangle + \beta \mu \nabla (\nabla \cdot \langle \boldsymbol{v_2} \rangle) - \langle \nabla p_2 \rangle = \langle \rho_1 \partial_t \boldsymbol{v_1} \rangle + \rho_f \langle (\boldsymbol{v_1} \cdot \nabla) \boldsymbol{v_1} \rangle$$

It can be observed that the second-order fields, as expressed on the left side of the equation, are dictated by the first-order fields found on the right side.

2. Particle Tracing Mechanism and Method

When the bulk acoustic waves propagate towards the microcavity chip and the PDMS-glass dish, the PMMA particles or cells experience two acoustic forces: an acoustic radiation force (ARF) caused by the scattering of sound waves on the objects, and a Stokes drag force generated by acoustic streaming. In the case where the size of the microscale objects is significantly smaller than the wavelength of the acoustic waves, the ARF acting on the microscale objects can be estimated using the following expressions [3]:

$$\boldsymbol{F_{rad}} = -\nabla \boldsymbol{U_{rad}} \tag{1}$$

$$\boldsymbol{U_{rad}} = \frac{4\pi}{3} {R_{mo}}^3 \left[f_1 \frac{1}{2} k_{mo} \langle p^2 - f_2 \frac{3}{4} \rho_{mo} \langle \boldsymbol{v}^2 \rangle \rangle \right] \tag{2}$$

$$f_1 = 1 - \frac{k_{mo}}{k_s} \tag{3}$$

$$f_2 = \frac{2\left(\frac{\rho_{mo}}{\rho_s} - 1\right)}{2\frac{\rho_{mo}}{\rho_s} + 1} \tag{4}$$

Where $\boldsymbol{F_{rad}}$ denotes the ARF, $\boldsymbol{U_{rad}}$ denotes the acoustic potential energy, R_{mo} denotes the radius of the microscale object, and p and $\boldsymbol{v}$ denote the first-order acoustic pressure and velocity, denting the microscale object and the surrounding medium, respectively.

For a minimal Reynolds number, the Stokes drag force $\boldsymbol{F_d}$ acting on the microscale objects can be described by the following formula [4]:

$$\boldsymbol{F_d} = 6\pi\eta R_{mo}\boldsymbol{v} \tag{5}$$

Where η is the dynamic viscosity, $\boldsymbol{v_2}$ is the time-averaged velocity of acoustic microstreaming. Consistent with Eqn. (2), (3) and (4), it is anticipated that both the ARF and drag forces will exert greater influence on larger microscale objects. Consequently, when subjected to similar acoustic vibrations, larger objects can be captured more easily compared to smaller ones. This enables the achievement of non-contact tunable multifunctional micromanipulation through the combined effects of these forces.

3. Acoustic radiation force and drag force on cells in microstreaming vortices

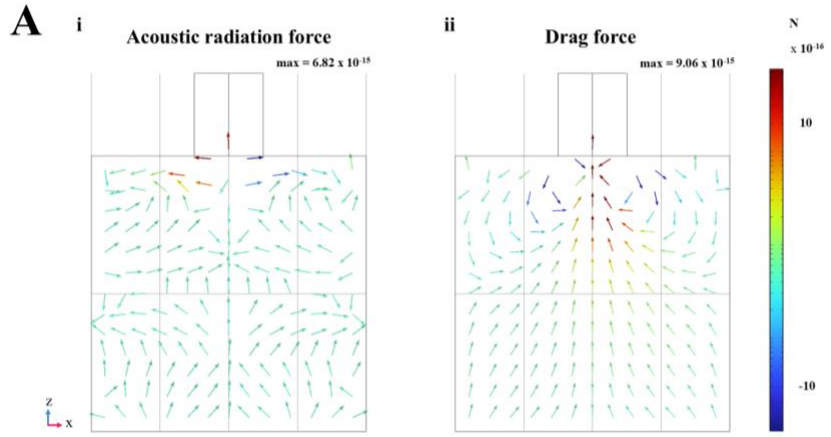

Figure S1. A. Acoustic radiation force distribution on the microstructure excited by vibration, simulated using COMSOL Multiphysics. **B.** Drag force distribution induced by acoustic streaming around the vibrating microstructure, obtained from COMSOL simulation. The color map shows the magnitude of the drag force (unit: N), and the streamlines represent the flow field pattern. The inset shows a detailed view of the force distribution near the critical regions.

Based on the models proposed by Muller et al. [1] and Karlsen et al. [5], numerical simulations were performed using COMSOL Multiphysics, with results shown in Figure S1. Within the microstreaming vortices, cells are simultaneously subjected to acoustic radiation force and drag force [6-9]. The drag force is calculated by integrating the shear stress over the cell surface. Simulation results indicate that the maximum drag force experienced by the cell is 9.06×10^{-15} N. Through the conversion between N and Pa (assuming a cell diameter of 15 μm), the maximum shear stress is determined to be 5.12×10^{-5} Pa. The calculation formula is as follows:

$$F = \tau \times A \tag{6}$$

$$A = \pi r^2 \tag{7}$$

$$\tau_{max} = F_{max} / (\pi r^2) \tag{8}$$

where **F** represents the drag force, **τ** denotes the shear stress, and **A** is the projected area of the cell.

The calculated shear stress value is substantially lower than the typical mechanical stimulation threshold for cells (0.1-10 Pa) [10-13], suggesting that shear forces of this magnitude have minimal impact on the physiological state of the cells.

Table 1. Comparison of Various Cell Manipulation and Bioprinting Methods

Technique		Advantage	Disadvantage	Throughput	Single cell Manipulation (Y/N)	Cell viability	Resolution
Cell sheet transfer	**Pipettes** [14-18]	Easy to perform; No special equipment needed.	Operator variability risk; Slow for large constructs.	1×10^6 cells / mm^2 [19]	N	-	-
				~ 200-850 cells / mm^2 [20]	N	-	-
	Forceps [21]			10×10 mm / per cell sheet [21]	N	-	-
	Gel-coated manipulators [22-24]	Accurate layer placement; Quick stacking process	Requires specific tools; More technical skill required	35mm / per cell sheet [22]	N	-	20-60 μm
				35mm / per cell sheet [25]	N	-	-
	Support membranes [26-28]	Provides stability; Allows thicker tissues	Requires additional materials; More expensive materials	Transfer yield ~ 71-81% [29]	N	96%	-
				Transfer area 10×10 mm^2 [30]	N	90%	-
Selective cell transfer printing [31, 32]		Short processing time; Low cost	Requires a mold; Insufficient control of pattern width and depth	~ 121 cells / mm^2 [33]	Y	93-97%	9-70 μm
				-	N	-	10 μm [34]
				~ 50-200 cells / mm^2 [35]	Y	-	-
Microcontact printing	**Soft lithography** [36-38]	Rapid prototyping	Challenge to control the ink	High-throughput ~ 400 cells / mm^2 [36]	Y	-	50 μm
				-	N	-	70-270 μm [37]
				~ 40 cells / mm^2 [39]	Y	-	10 μm
				~ 50-400 cells / mm^2 [43]	N	-	40-200 μm
Stencil-based	**Physical barriers** [40-42]	Decrease the surface chemistry	Complicated fabrication process	High-throughput ~ 324 cells / mm^2 [44]	Y	-	8-400 μm
				High-throughput ~ 1000 microbowls / mm^2 [45]	N	>95%	30 μm
External fields	**Electrical** [46-48]	Easy trapping cells by regulating the frequency of AC	Require specialized electrode equipment	High-throughput ~ 380 cells / mm^2 [49]	Y	-	20 μm
				High-throughput ~ 1000 cells / mm^2 [50]	N	-	-
	Optical [51-53]	Specific manipulation to the cells with dielectric properties	Large power output required to trap cells may damage cells due to heating	1 cell [54]	Y	-	-
				1 cell [55]	Y	-	-
	Magnetic [56-58]	Remote manipulation;	Require magnets and labelling cells	High-throughput ~ 336 cells / mm^2 [59]	Y	-	15 μm

		Efficient trapping of labeled cells	with magnetic particles	~ 16 cells / mm^2 [60]	Y	>95%	150 μm
	Hydrodynamic [61-63]	Multifunction in one device.	The shear stress may affect the function of cells.	High-throughput ~ 512 cells / per operation [64]	Y	-	20 μm
				High-throughput ~ 300 cells / mm^2 [65]	Y	100%	5 μm
	Acoustic [66-68]	lower power with no damage to cell viability.	Require piezoelectric surface specialized.	High-throughput, ~ 100 pairs / 30 min [69]	Y	-	5-20 μm
	Extrusion-based [25, 48, 70]	Wide range of biomaterical can be selected for printing; Porous complex models can be printed.	Pressure is generally increased causing low cell viability; Sometimes high temperature is not good for cells.	3×10^4-3.6×10^5 cells / min [71]	N	>95%	-
				1-1.05×10^5 cells / min [72]	N	>90%	-
Bioprinting	**Jetting-based** [25, 48, 70]	Easy modification; Simple operation; Concentration can be varied.	The size is enormous. Limited variety of bioink.	High-Throughput 48 droplets/min (4750 cells/droplet) [73]	N	-	20 μm
				High-Throughput 4.488×10^5 cells / min [74]	N	>99.8	-
	Vat polymerization-based [75, 76]	High precision and complexity; Reduced material waste	Material Limitation; Mechanical performance limitations.	High-Throughput 2.18×10^4-2.18×10^6 cells / min [77]	N	>90%	200 μm
				4×10^4-4×10^6 cells / min [78]	N	>90%	38-300 μm

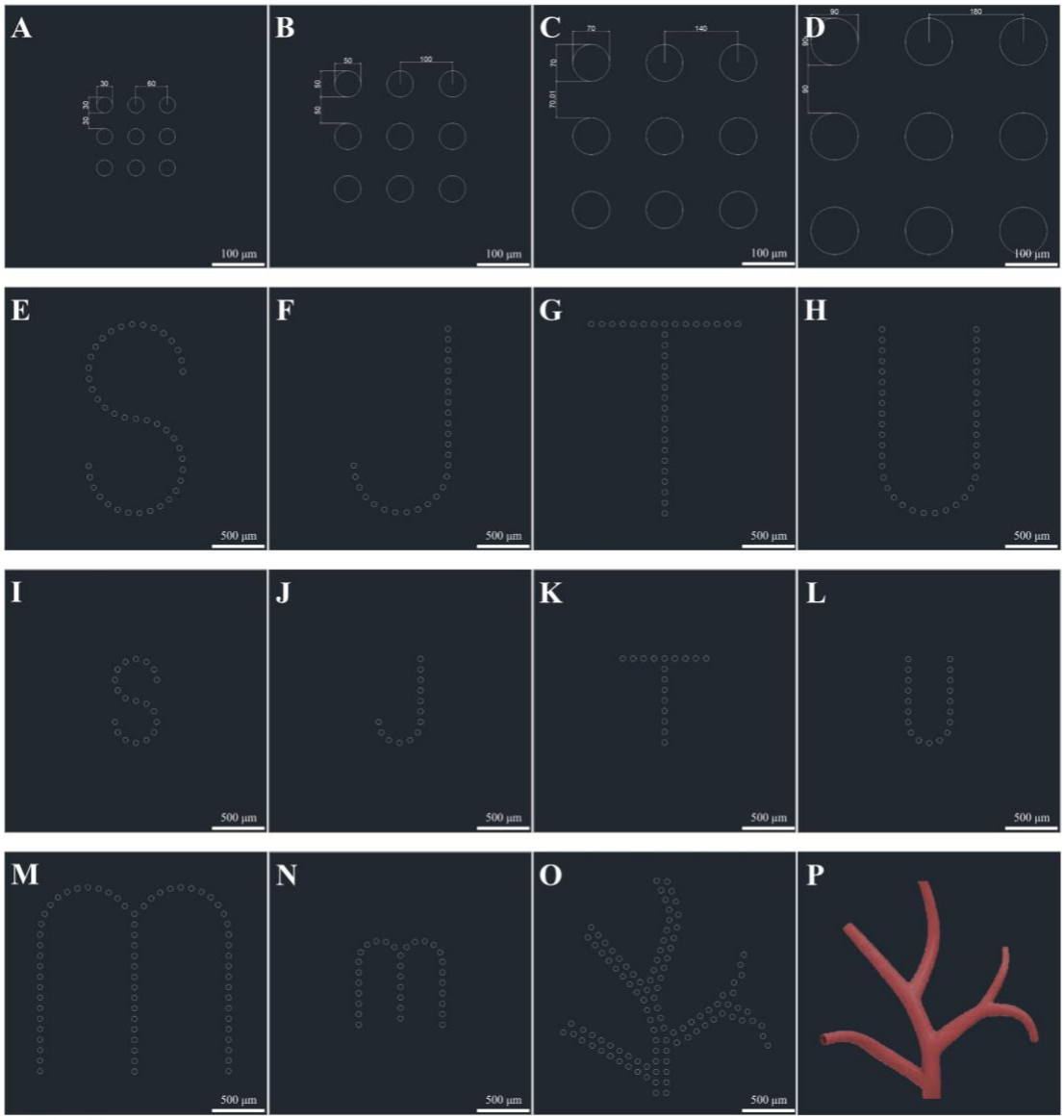

Figure S2. A part of the microcavity array with **(A)** diameter=30 µm, **(B)** diameter=50 µm, **(C)** diameter=70 µm, and **(D)** diameter=90 µm. Scale bar: 100 µm. **(E - H, and M)** The patterning microcavity pattern chip for particle trapping. **(I - L, N, and O)** The patterning microcavity pattern chip for cell trapping. Scale bar: 500 µm. **P.** The target pattern is used in the acoustic hologram design.

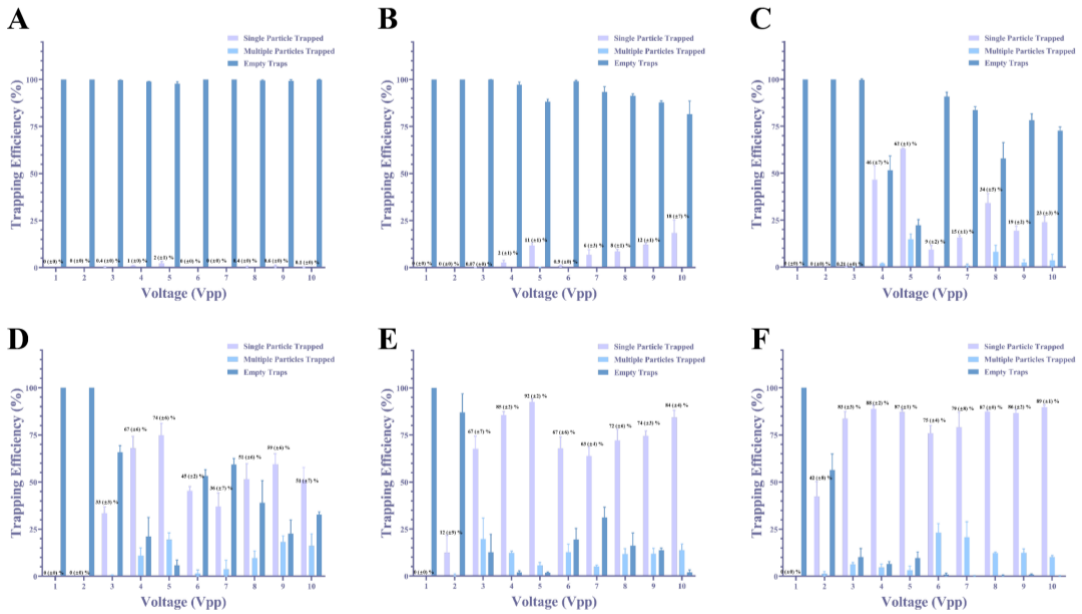

Figure S3. PMMA particles trapping efficiency with microcavity array chip (diameter = 50 µm), at 1 - 10 Vpp, **(A)** 500 Hz, **(B)** 600 Hz, **(C)** 700 Hz, **(D)** 800 Hz, **(E)** 900 Hz, and **(F)** 1000 Hz.

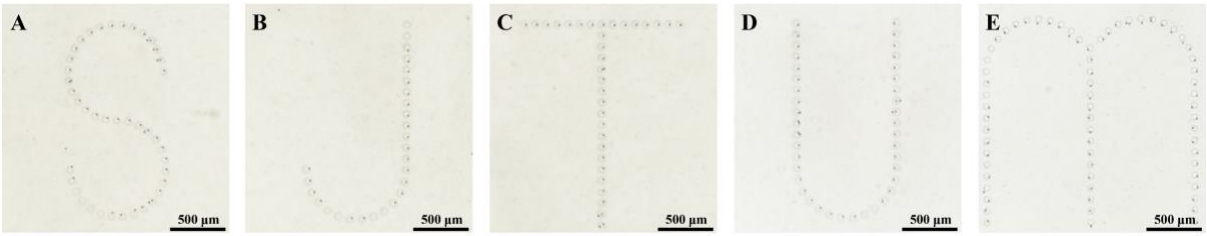

Figure S4. A. Microscopic images of PMMA particles trapping with pattern microcavity chip (diameter=50 μm). The patterns were "S", "J", "T", "U", and "M", respectively. The vibrations were 900 Hz, 5 Vpp. Scale bar: 500 μm.

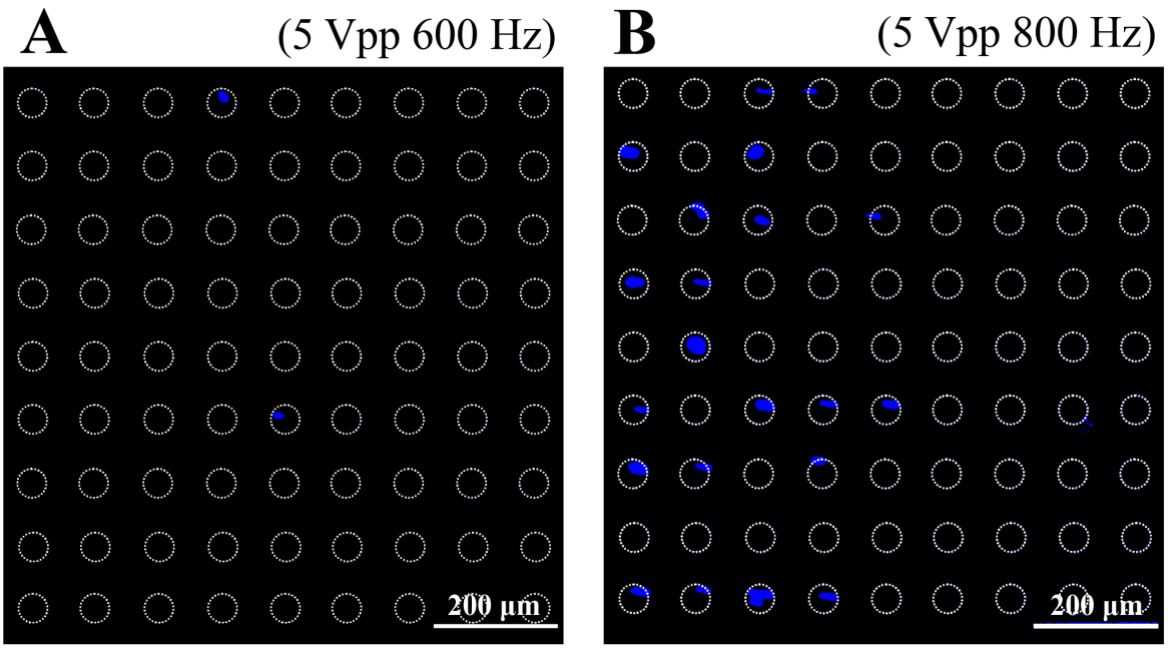

Figure S5. Immunofluorescence images of trapped cells. The vibration conditions were 600 **(A)** and 800 **(B)** Hz, 5 Vpp. Scale bar: 200 μm.

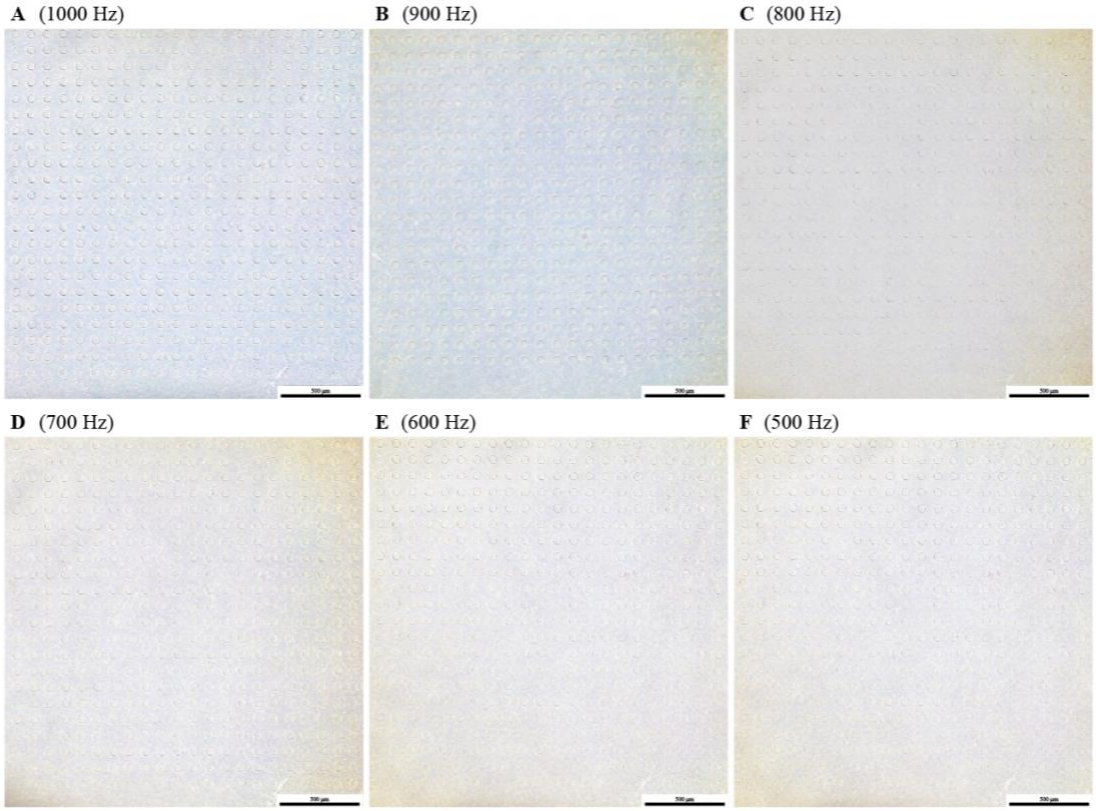

Figure S6. Microscopic images of experimental PMMA particles trapped in the microcavity array chip at 1 Vpp with different frequency, **(A)** 1000 Hz, **(B)** 900 Hz, **(C)** 800 Hz, **(D)** 700 Hz, **(E)** 600 Hz and **(F)** 500 Hz. Scale bar: 500 μm.

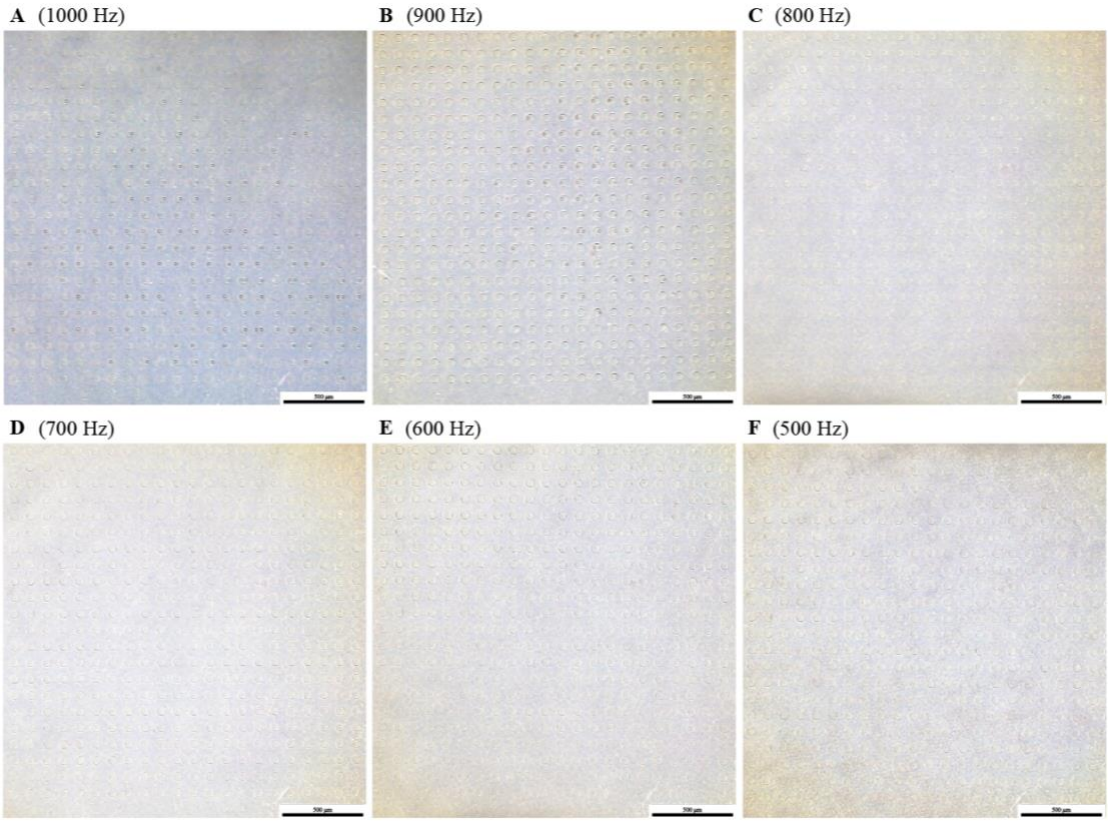

Figure S7. Microscopic images of experimental PMMA particles trapped in the microcavity array chip at 2 Vpp with different frequency, **(A)** 1000 Hz, **(B)** 900 Hz, **(C)** 800 Hz, **(D)** 700 Hz, **(E)** 600 Hz and **(F)** 500 Hz. Scale bar: 500 μm.

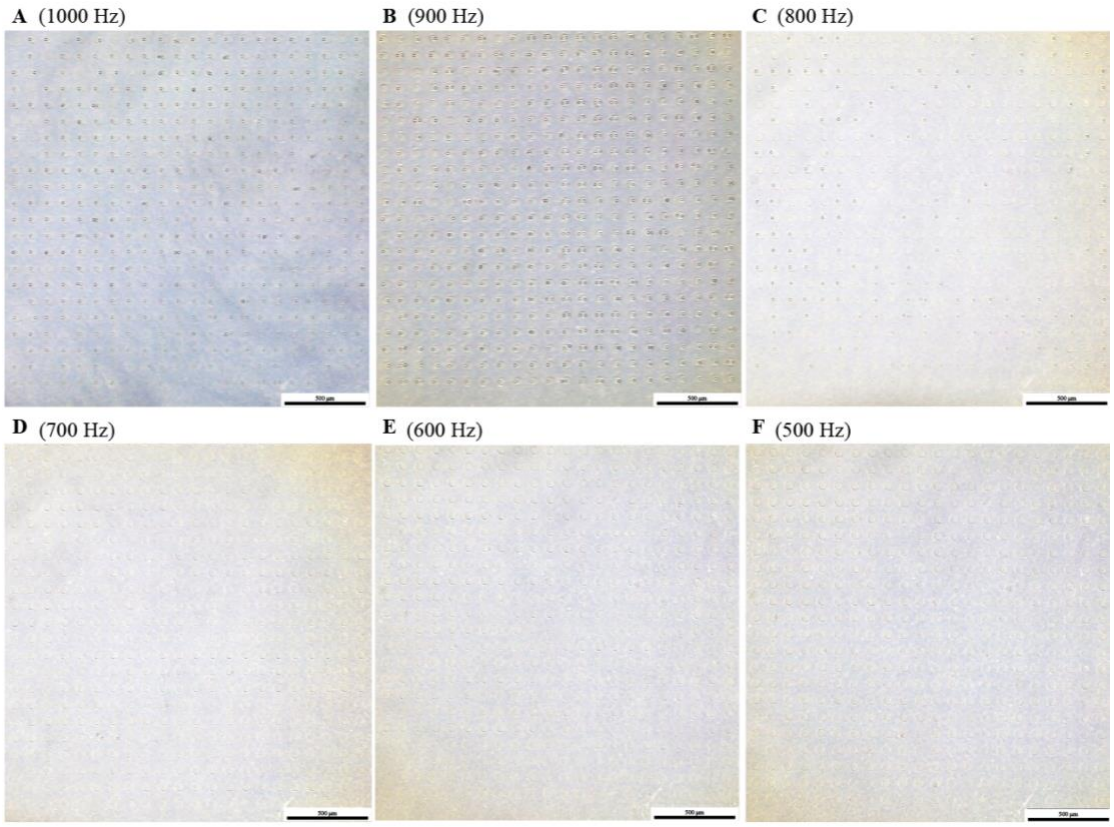

Figure S8. Microscopic images of experimental PMMA particles trapped in the microcavity array chip at 3 Vpp with different frequency, **(A)** 1000 Hz, **(B)** 900 Hz, **(C)** 800 Hz, **(D)** 700 Hz, **(E)** 600 Hz and **(F)** 500 Hz. Scale bar: 500 μm.

v

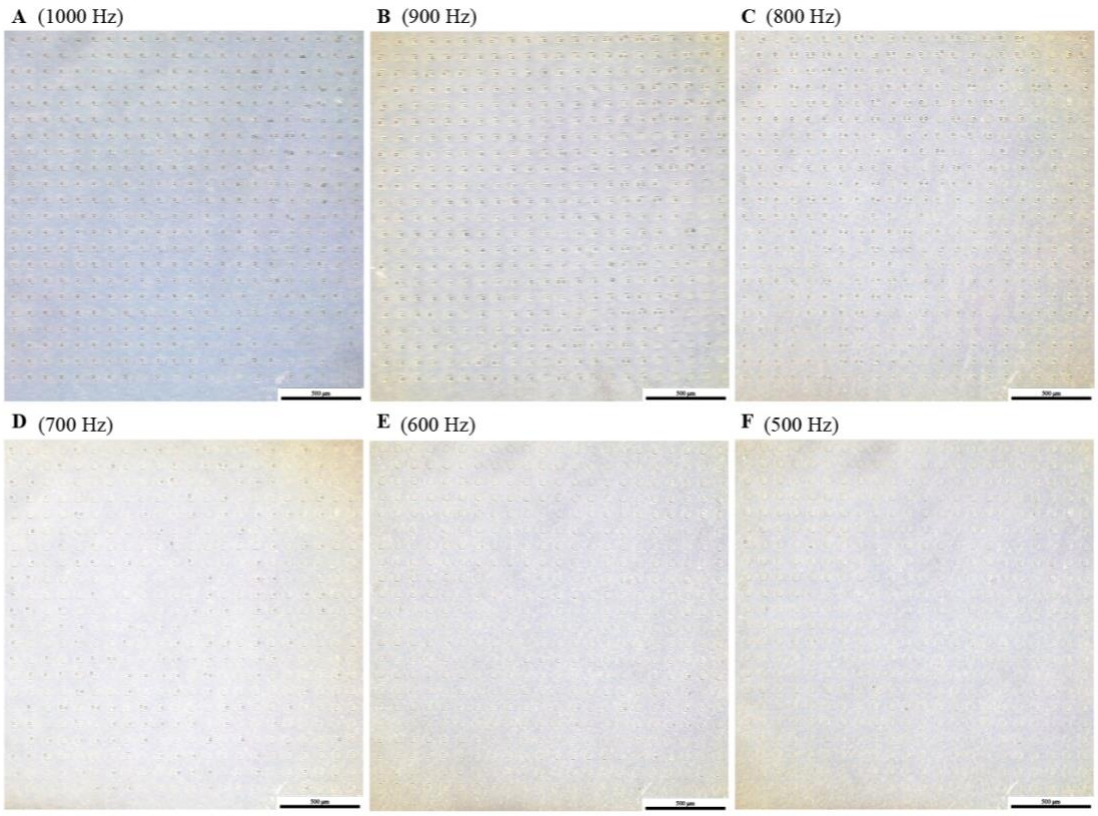

Figure S9. Microscopic images of experimental PMMA particles trapped in the microcavity array chip at 4 Vpp with different frequency, **(A)** 1000 Hz, **(B)** 900 Hz, **(C)** 800 Hz, **(D)** 700 Hz, **(E)** 600 Hz and **(F)** 500 Hz. Scale bar: 500 μm.

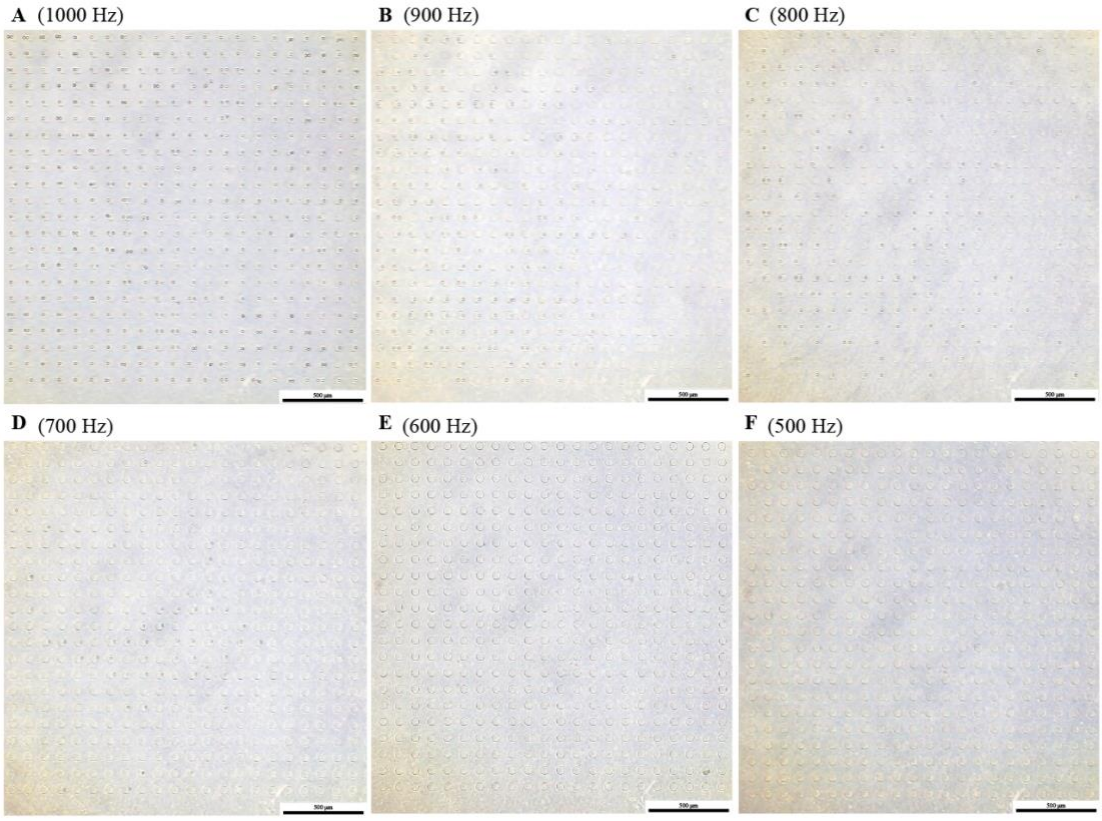

Figure S10. Microscopic images of experimental PMMA particles trapped in the microcavity array chip at 6 Vpp with different frequency, **(A)** 1000 Hz, **(B)** 900 Hz, **(C)** 800 Hz, **(D)** 700 Hz, **(E)** 600 Hz and **(F)** 500 Hz. Scale bar: 500 μm.

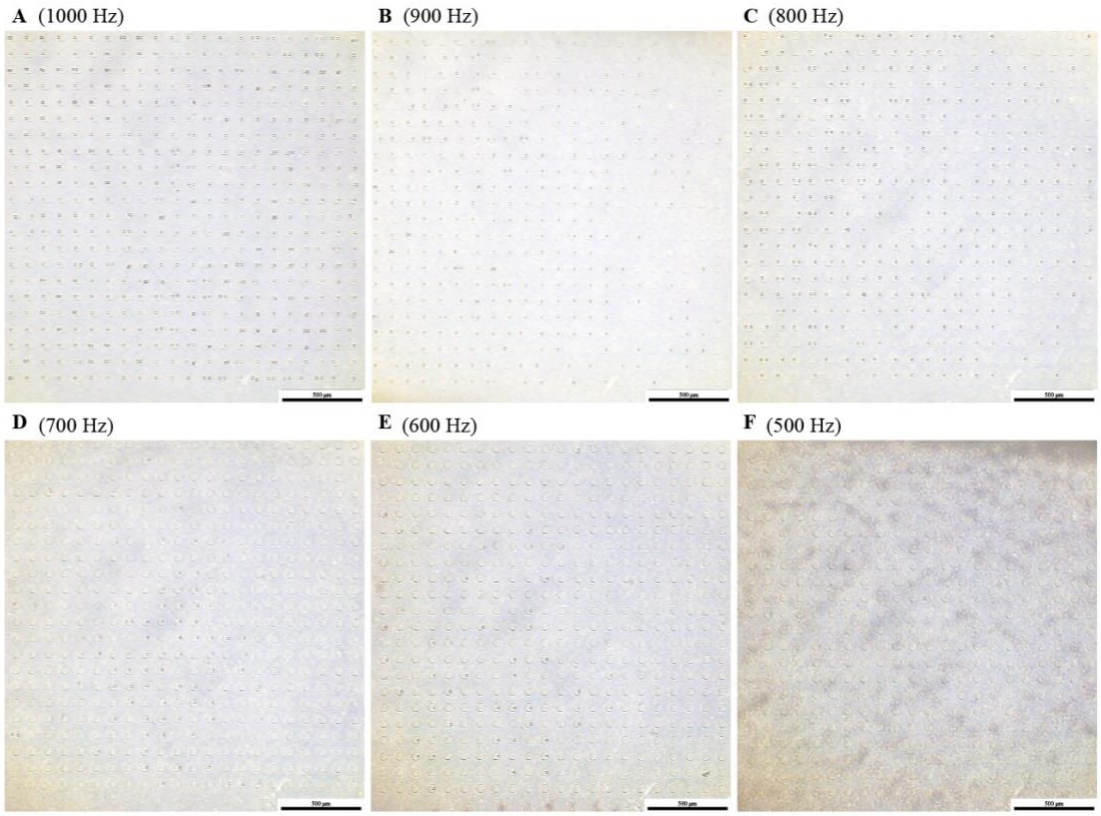

Figure S11. Microscopic images of experimental PMMA particles trapped in the microcavity array chip at 7 Vpp with different frequency, **(A)** 1000 Hz, **(B)** 900 Hz, **(C)** 800 Hz, **(D)** 700 Hz, **(E)** 600 Hz and **(F)** 500 Hz. Scale bar: 500 μm.

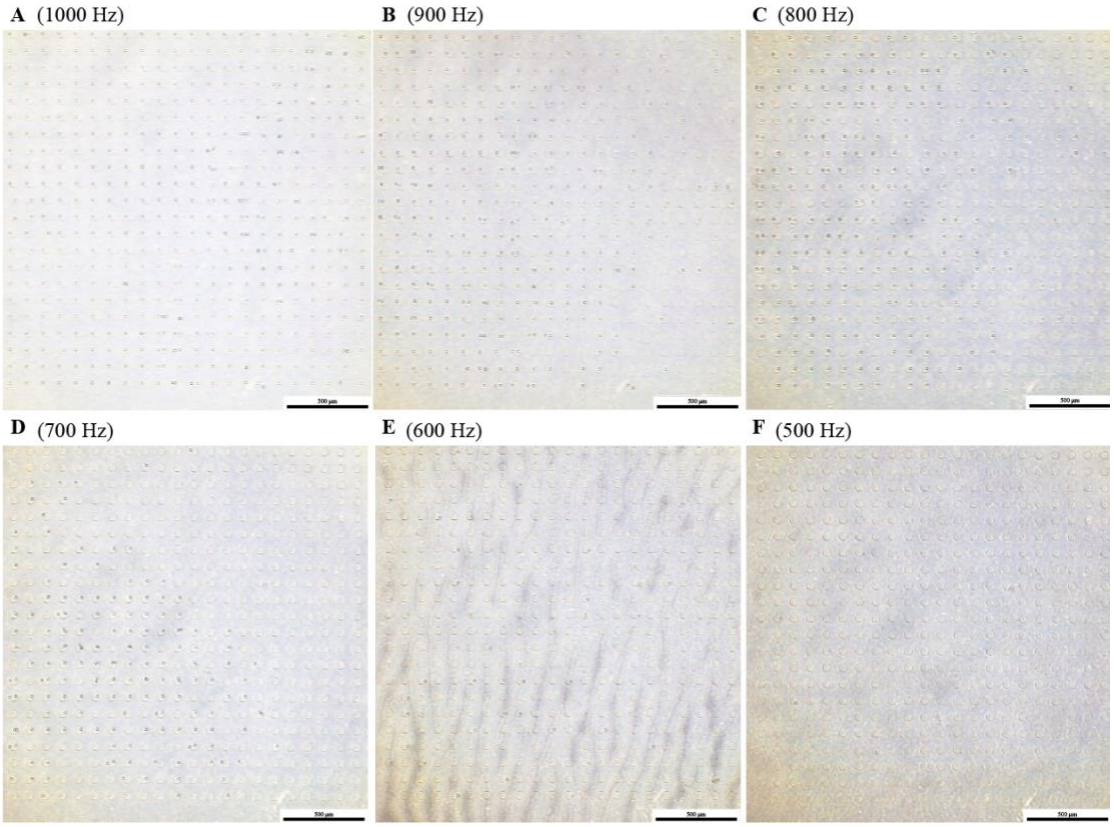

Figure S12. Microscopic images of experimental PMMA particles trapped in the microcavity array chip at 8 Vpp with different frequency, **(A)** 1000 Hz, **(B)** 900 Hz, **(C)** 800 Hz, **(D)** 700 Hz, **(E)** 600 Hz and **(F)** 500 Hz. Scale bar: 500 μm.

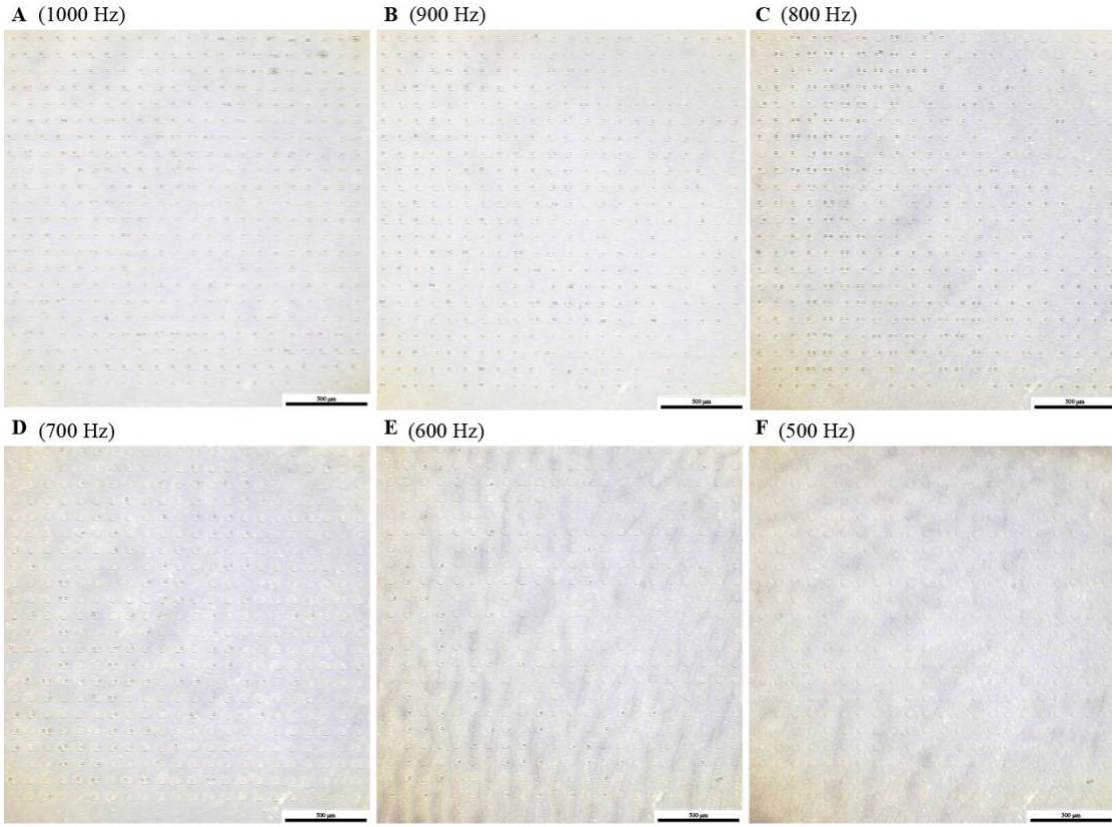

Figure S13. Microscopic images of experimental PMMA particles trapped in the microcavity array chip at 9 Vpp with different frequency, **(A)** 1000 Hz, **(B)** 900 Hz, **(C)** 800 Hz, **(D)** 700 Hz, **(E)** 600 Hz and **(F)** 500 Hz. Scale bar: 500 μm.

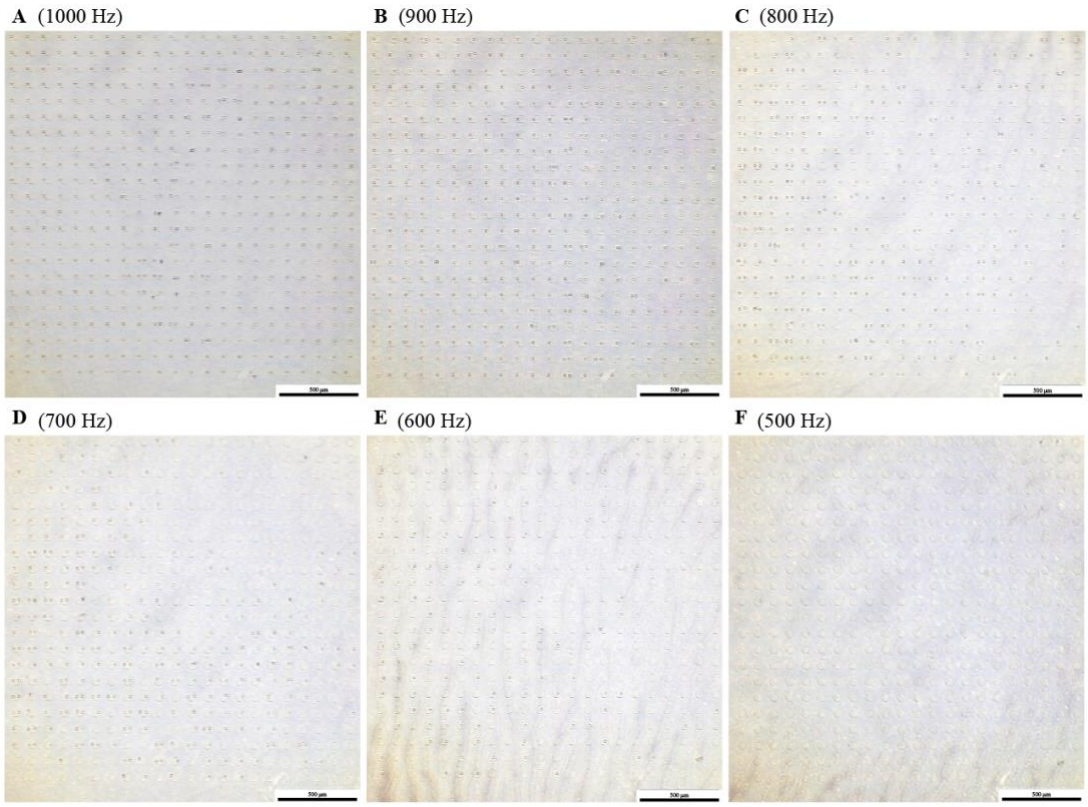

Figure S14. Microscopic images of experimental PMMA particles trapped in the microcavity array chip at 10 Vpp with different frequency, **(A)** 1000 Hz, **(B)** 900 Hz, **(C)** 800 Hz, **(D)** 700 Hz, **(E)** 600 Hz and **(F)** 500 Hz. Scale bar: 500 μm.

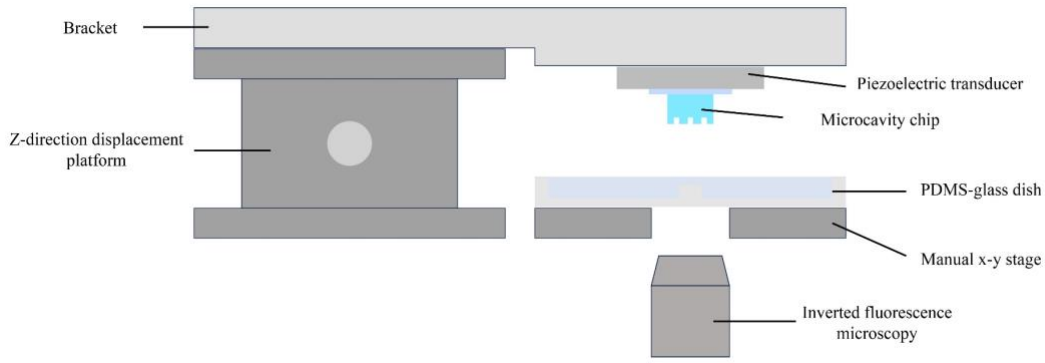

Figure S15. Schematic representation of the bioadhesion-free cellular transfer printing system.

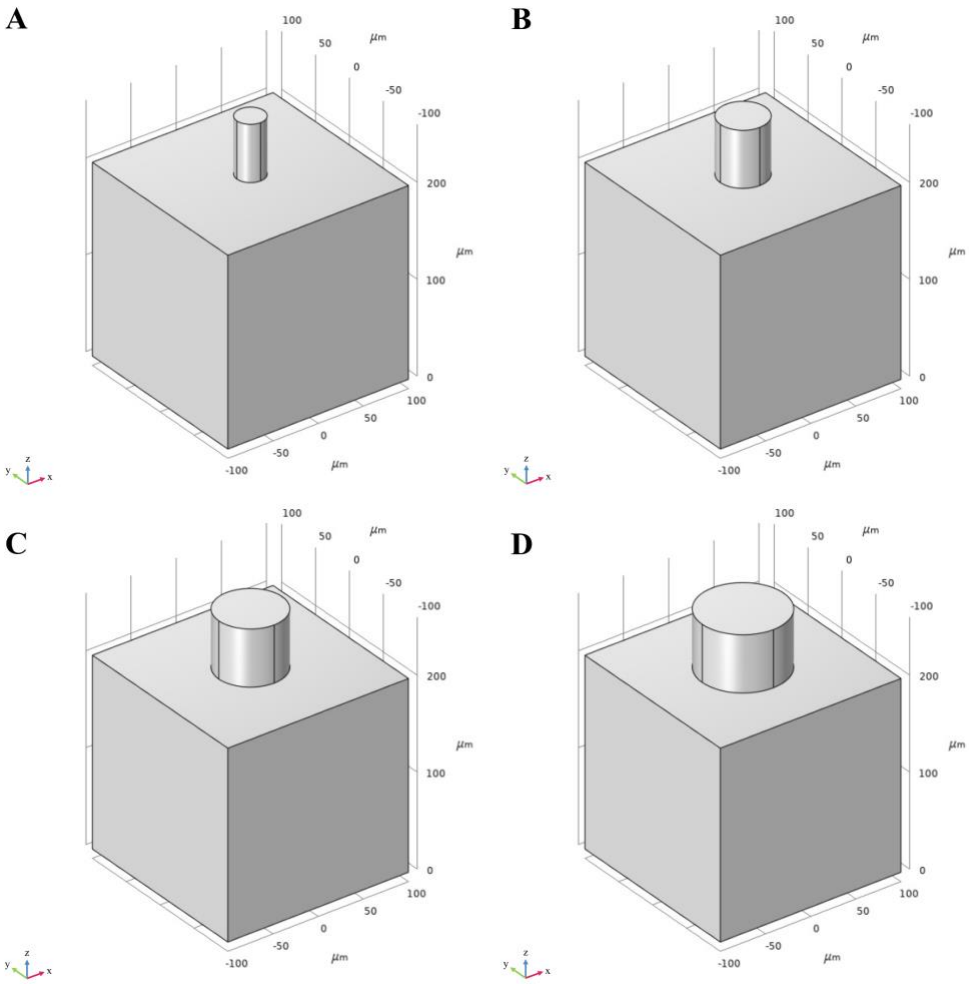

Figure S16. The actual dimensions of the microcavity structure along the X-Y-Z plane were applied in the FEM model. **(A)** 30 μm, **(B)** 50 μm, **(C)** 70 μm, and **(D)** 90 μm.

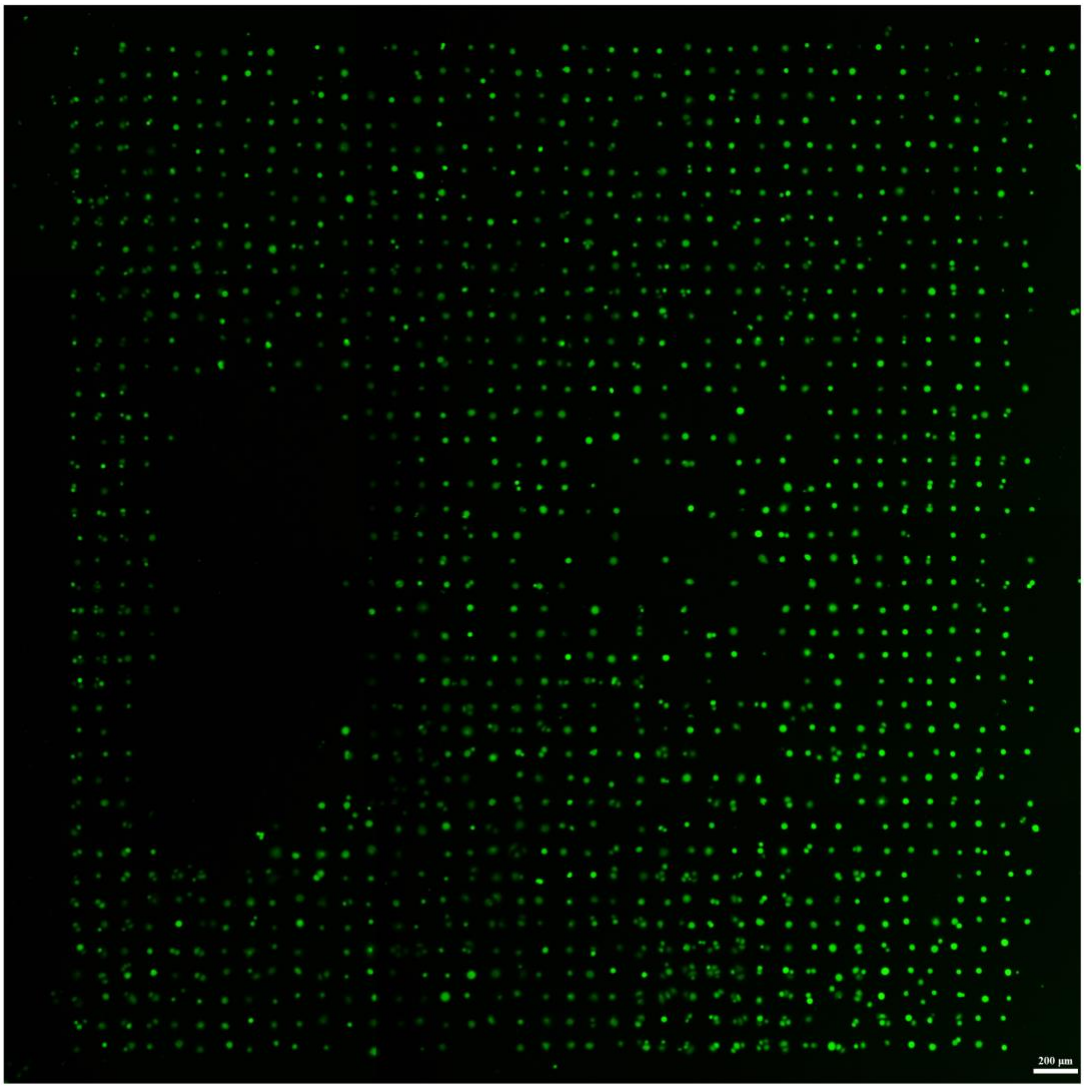

Figure S17. Experimental visualization of cellular entrapment within a 42×42 microcavity array (microcavity with 50 μm diameter). After adhesion, the cells were fluorescently labeled with Calcein AM to enhance observational clarity.

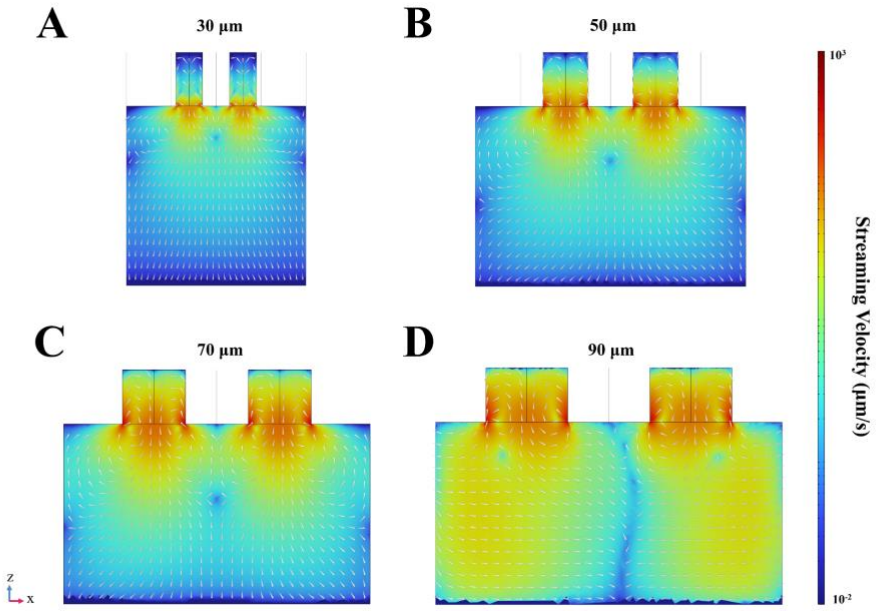

Figure S18. Numerical simulation of microstreaming velocity fields generated by neighboring microcavities. (**A-D**) Velocity distribution maps showing the microstreaming patterns induced by dual identical microcavities with diameters of 30 μm, 50 μm, 70 μm, and 90 μm, respectively. The inter-cavity spacing was set equal to the microcavity diameter in each configuration. Color maps represent the microstreaming velocity magnitude (μm/s).

Comparative analysis of numerical simulations between single-microcavity and dual-microcavity configurations revealed distinct microstreaming patterns dependent on microcavity dimensions. For microcavities with diameters of 30 μm, 50 μm, and 70 μm, the presence of neighboring microcavities primarily manifested in reduced microvortex dimensions while maintaining their morphological characteristics. However, a notable transition in flow behavior was observed in the 90-μm-diameter cavity configuration, where the proximity of adjacent cavities induced significant morphological alterations in the microvortex structure. This phenomenon suggests that the interaction between neighboring microcavities becomes increasingly pronounced as the microcavity diameter increases.

References

1. P. B. Muller, R. Barnkob, M. J. Jensen and H. Bruus, *Lab Chip*, 2012, **12**, 4617-4627.
2. H. Bruus, *Lab Chip*, 2012, **12**, 1014-1021.
3. H. Ahmed, S. Ramesan, L. Lee, A. R. Rezk and L. Y. Yeo, *Small*, 2020, **16**, e1903605.
4. X. Lu, K. Zhao, H. Peng, H. Li and W. Liu, *Phys. Rev. Appl.*, 2019, **11**, 044064.
5. Jonas T. Karlsen and H. Bruus, *Phys Rev E*, 2015, **92**.
6. J. Wu, *Fluids*, 2018, **3**.
7. L. A. Kuznetsova and W. T. Coakley, *Biosens Bioelectron*, 2007, **22**, 1567-1577.
8. A. Pavlic, P. Nagpure, L. Ermanni and J. Dual, *Phys Rev E*, 2022, **106**, 015105.
9. W. Wei, Y. Wang, Z. Wang and X. Duan, *TrAC Trends in Analytical Chemistry*, 2023, **160**.
10. B. Martinac, Y. A. Nikolaev, G. Silvani, N. Bavi, V. Romanov, Y. Nakayama, A. D. Martinac, P. Rohde, O. Bavi and C. D. Cox, *Curr Top Membr*, 2020, **86**, 83-141.
11. W. Xi, T. B. Saw, D. Delacour, C. T. Lim and B. Ladoux, *Nature Reviews Materials*, 2018, **4**, 23-44.
12. B. K. Walther, N. K. Rajeeva Pandian, K. A. Gold, E. S. Kilic, V. Sama, J. Gu, A. K. Gaharwar, A. Guiseppi-Elie, J. P. Cooke and A. Jain, *Lab Chip*, 2021, **21**, 1738-1751.
13. M. Cantini, H. Donnelly, M. J. Dalby and M. Salmeron-Sanchez, *Adv Healthc Mater*, 2020, **9**, e1901259.
14. H. Sekine, T. Shimizu, S. Kosaka, E. Kobayashi and T. Okano, *J Heart Lung Transplant*, 2006, **25**, 324-332.
15. H. Sekine, T. Shimizu, I. Dobashi, K. Matsuura, N. Hagiwara, M. Takahashi, E. Kobayashi, M. Yamato and T. Okano, *Tissue Eng Part A*, 2011, **17**, 2973-2980.
16. T. Shimizu, M. Yamato, Y. Isoi, T. Akutsu, T. Setomaru, K. Abe, A. Kikuchi, M. Umezu and T. Okano, *Circ Res*, 2002, **90**, e40.
17. T. Shimizu, H. Sekine, Y. Isoi, M. Yamato, A. Kikuchi and T. Okano, *Tissue Eng*, 2006, **12**, 499-507.
18. A. Arauchi, T. Shimizu, M. Yamato, T. Obara and T. Okano, *Tissue Eng Part A*, 2009, **15**, 3943-3949.
19. G. Forte, S. Pietronave, G. Nardone, A. Zamperone, E. Magnani, S. Pagliari, F. Pagliari, C. Giacinti, C. Nicoletti, A. Musaro, M. Rinaldi, M. Ribezzo, C. Comoglio, E. Traversa, T. Okano, M. Minieri, M. Prat and P. Di Nardo, *Stem Cells*, 2011, **29**, 2051-2061.
20. H. Sekine, T. Shimizu, K. Hobo, S. Sekiya, J. Yang, M. Yamato, H. Kurosawa, E. Kobayashi and T. Okano, *Circulation*, 2008, **118**, S145-152.
21. L. Shi, B. C. Tee, L. Cotter and Z. Sun, *Aesthetic Plast Surg*, 2020, **44**, 191-200.
22. Y. Tsuda, T. Shimizu, M. Yamato, A. Kikuchi, T. Sasagawa, S. Sekiya, J. Kobayashi, G. Chen and T. Okano, *Biomaterials*, 2007, **28**, 4939-4946.
23. N. Asakawa, T. Shimizu, Y. Tsuda, S. Sekiya, T. Sasagawa, M. Yamato, F. Fukai and T. Okano, *Biomaterials*, 2010, **31**, 3903-3909.
24. T. Sasagawa, T. Shimizu, S. Sekiya, Y. Haraguchi, M. Yamato, Y. Sawa and T. Okano, *Biomaterials*, 2010, **31**, 1646-1654.
25. A. Memic, A. Navaei, B. Mirani, J. A. V. Cordova, M. Aldhahri, A. Dolatshahi-Pirouz, M. Akbari and M. Nikkhah, *Biotechnol Lett*, 2017, **39**, 1279-1290.
26. K. Nishida, M. Yamato, Y. Hayashida, K. Watanabe, N. Maeda, H. Watanabe, K. Yamamoto, S. Nagai, A. Kikuchi, Y. Tano and T. Okano, *Transplantation*, 2004, **77**, 379-385.
27. K. Ohashi, T. Yokoyama, M. Yamato, H. Kuge, H. Kanehiro, M. Tsutsumi, T. Amanuma, H. Iwata, J. Yang, T. Okano and Y. Nakajima, *Nat Med*, 2007, **13**, 880-885.

28. T. Iwata, M. Yamato, H. Tsuchioka, R. Takagi, S. Mukobata, K. Washio, T. Okano and I. Ishikawa, *Biomaterials*, 2009, **30**, 2716-2723.
29. M. Kawecki, M. Kraut, A. Klama-Baryla, W. Labus, D. Kitala, M. Nowak, J. Glik, A. L. Sieron, A. Utrata-Wesolek, B. Trzebicka, A. Dworak and D. Szweda, *J Mater Sci Mater Med*, 2016, **27**, 111.
30. S. Hong, B. Y. Jung and C. Hwang, *Tissue Eng Regen Med*, 2017, **14**, 371-381.
31. M. Kim, D. Ha and T. Kim, *Nat Commun*, 2015, **6**, 6247.
32. H. H. Hwang, W. Zhu, G. Victorine, N. Lawrence and S. Chen, *Small Methods*, 2018, **2**.
33. D. Ayibaike, M. Cui and J. Wei, *Applied Sciences*, 2018, **8**.
34. K. Itoga, J. Kobayashi, M. Yamato, A. Kikuchi and T. Okano, *Biomaterials*, 2006, **27**, 3005-3009.
35. S. Yu, X. Zuo, T. Shen, Y. Duan, Z. Mao and C. Gao, *Acta Biomater*, 2018, **72**, 70-81.
36. M. Garcia-Hernando, A. Calatayud-Sanchez, J. Etxebarria-Elezgarai, M. M. de Pancorbo, F. Benito-Lopez and L. Basabe-Desmonts, *Anal Chem*, 2020, **92**, 9658-9665.
37. A. J. Khadpekar, M. Khan, A. Sose and A. Majumder, *Sci Rep*, 2019, **9**, 1024.
38. Y. Miao, H. Liu, W. Cheng, Y. Liu, S. Kim, X. Yuan, A. Kusi-Appiah, S. Lenhert, T. Ma, Y. Ren, H. Chung and J. Guan, *ACS Appl Mater Interfaces*, 2020, **12**, 29110-29121.
39. H. Wu, L. Wu, X. Zhou, B. Liu and B. Zheng, *Small*, 2018, **14**, e1802128.
40. L. Huang, Y. Chen, L. T. Weng, M. Leung, X. Xing, Z. Fan and H. Wu, *Anal Chem*, 2016, **88**, 12196-12203.
41. Y. Jimbo, H. P. Robinson and A. Kawana, *IEEE Trans Biomed Eng*, 1993, **40**, 804-810.
42. K. F. Zaidi and N. Agrawal, *Biomicrofluidics*, 2018, **12**, 064104.
43. D. Wright, B. Rajalingam, S. Selvarasah, M. R. Dokmeci and A. Khademhosseini, *Lab Chip*, 2007, **7**, 1272-1279.
44. J. Wu, M. Zhang, L. Chen, V. Yu, J. Tin-Yum Wong, X. Zhang, J. Qin and W. Wen, *RSC Advances*, 2011, **1**.
45. L. Xu, X. Li, W. Li, K. C. Chang, H. Yang, N. Tao, P. Zhang, E. M. Payne, C. Modavi, J. Humphries, C. W. Lu and A. R. Abate, *Adv Mater*, 2022, **34**, e2108194.
46. M. Antfolk, S. H. Kim, S. Koizumi, T. Fujii and T. Laurell, *Sci Rep*, 2017, **7**, 46507.
47. K. Huang, H. K. Chu, B. Lu and L. Cheng, presented in part at the 2018 IEEE International Conference on Robotics and Biomimetics (ROBIO), 2018.
48. J. M. Lee and W. Y. Yeong, *Adv Healthc Mater*, 2016, **5**, 2856-2865.
49. S. H. Kim, T. Yamamoto, D. Fourmy and T. Fujii, *Small*, 2011, **7**, 3239-3247.
50. P. Gascoyne, C. Mahidol, M. Ruchirawat, J. Satayavivad, P. Watcharasit and F. Becker, *Lab Chip*, 2002, **2**, 70-75.
51. A. Keloth, O. Anderson, D. Risbridger and L. Paterson, *Micromachines (Basel)*, 2018, **9**.
52. Y. Liang, G. Liang, Y. Xiang, J. Lamstein, R. Gautam, A. Bezryadina and Z. Chen, *Physical Review Applied*, 2019, **12**.
53. X. Dong, R. Hu, T. Wei, S. Chen and S. Hu, presented in part at the 2019 IEEE/ASME International Conference on Advanced Intelligent Mechatronics (AIM), 2019.
54. P. Jing, Y. Liu, E. G. Keeler, N. M. Cruz, B. S. Freedman and L. Y. Lin, *Biomed Opt Express*, 2018, **9**, 771-779.
55. Z. Zhang, T. E. P. Kimkes and M. Heinemann, *Sci Rep*, 2019, **9**, 19086.
56. T. C. Butler, J. Zhang, H. Zhang, S. Ryu and A. S. Greene, *J Eukaryot Microbiol*, 2020, **67**, 687-690.
57. I. Guryanov, E. Naumenko, S. Konnova, M. Lagarkova, S. Kiselev and R. Fakhrullin, *Nanomedicine*, 2019, **20**, 102038.

58. M. Bongaerts, K. Aizel, E. Secret, A. Jan, T. Nahar, F. Raudzus, S. Neumann, N. Telling, R. Heumann, J. M. Siaugue, C. Menager, J. Fresnais, C. Villard, A. El Haj, J. Piehler, M. A. Gates and M. Coppey, *Int J Mol Sci*, 2020, **21**.
59. N.-T. Huang, Y.-J. Hwong and R. L. Lai, *Microfluid. Nanofluid.*, 2018, **22**.
60. K. Ino, M. Okochi, N. Konishi, M. Nakatochi, R. Imai, M. Shikida, A. Ito and H. Honda, *Lab Chip*, 2008, **8**, 134-142.
61. C. Lu, J. Xu, J. Han, X. Li, N. Xue, J. Li, W. Wu, X. Sun, Y. Wang, Q. Ouyang, G. Yang and C. Luo, *Lab Chip*, 2020, **20**, 4094-4105.
62. M. S. Brugger, S. Grundeen, A. Doyle, L. Theogarajan, A. Wixforth and C. Westerhausen, *Phys Rev E*, 2018, **98**, 012411.
63. X. Chen, Z. Liang, D. Li, Y. Xiong, P. Xiong, Y. Guan, S. Hou, Y. Hu, S. Chen, G. Liu and Y. Tian, *Biosens Bioelectron*, 2018, **99**, 416-423.
64. T. Arakawa, M. Noguchi, K. Sumitomo, Y. Yamaguchi and S. Shoji, *Biomicrofluidics*, 2011, **5**, 14114.
65. K. Zhang, C. K. Chou, X. Xia, M. C. Hung and L. Qin, *Proc Natl Acad Sci U S A*, 2014, **111**, 2948-2953.
66. J. P. K. Armstrong, J. L. Puetzer, A. Serio, A. G. Guex, M. Kapnisi, A. Breant, Y. Zong, V. Assal, S. C. Skaalure, O. King, T. Murty, C. Meinert, A. C. Franklin, P. G. Bassindale, M. K. Nichols, C. M. Terracciano, D. W. Hutmacher, B. W. Drinkwater, T. J. Klein, A. W. Perriman and M. M. Stevens, *Adv Mater*, 2018, **30**, e1802649.
67. T. D. Nguyen, Y. Q. Fu, V.-T. Tran, A. Gautam, S. Pudasaini and H. Du, *Sensors and Actuators B: Chemical*, 2020, **318**.
68. S. Cohen, H. Sazan, A. Kenigsberg, H. Schori, S. Piperno, H. Shpaisman and O. Shefi, *Sci Rep*, 2020, **10**, 4932.
69. S. Yang, J. Rufo, R. Zhong, J. Rich, Z. Wang, L. P. Lee and T. J. Huang, *Nat Protoc*, 2023, **18**, 2441-2458.
70. S. V. Murphy and A. Atala, *Nat Biotechnol*, 2014, **32**, 773-785.
71. N. K. Singh, W. Han, S. A. Nam, J. W. Kim, J. Y. Kim, Y. K. Kim and D. W. Cho, *Biomaterials*, 2020, **232**, 119734.
72. S. Fathi, I. M. Lei, Y. Cao and Y. Y. S. Huang, *Biodes Manuf*, 2023, **6**, 1-11.
73. R. H. Utama, L. Atapattu, A. P. O'Mahony, C. M. Fife, J. Baek, T. Allard, K. J. O'Mahony, J. C. C. Ribeiro, K. Gaus, M. Kavallaris and J. J. Gooding, *iScience*, 2020, **23**, 101621.
74. P. Suwannakot, L. Zhu, M. A. K. Tolentino, E. Y. Du, A. Sexton, S. Myers and J. J. Gooding, *ACS Appl Bio Mater*, 2024, **7**, 269-283.
75. M. Pagac, J. Hajnys, Q. P. Ma, L. Jancar, J. Jansa, P. Stefek and J. Mesicek, *Polymers (Basel)*, 2021, **13**.
76. P. Fiedor, M. Pilch, P. Szymaszek, A. Chachaj-Brekiesz, M. Galek and J. Ortyl, *Catalysts*, 2020, **10**.
77. R. Rizzo, D. Ruetsche, H. Liu and M. Zenobi-Wong, *Adv Mater*, 2021, **33**, e2102900.
78. M. Wang, W. Li, L. S. Mille, T. Ching, Z. Luo, G. Tang, C. E. Garciamendez, A. Lesha, M. Hashimoto and Y. S. Zhang, *Adv Mater*, 2022, **34**, e2107038.